
Hermite integrator for high-order mesh-free schemes

Satoko YAMAMOTO^{1,2,3*} and Junichiro MAKINO,^{3,2,1}

¹Department of Earth & Planetary Sciences, Tokyo Institute of Technology, Ookayama, Meguro-ku, Tokyo 152-8550, Japan

²RIKEN Advanced Institute for Computational Science, Minatojima-minamimachi, Chuo-ku, Kobe, Hyogo 650-0047, Japan

³Department of Planetology, Kobe University, Rokkodaicho, Nada-ku, Kobe, Hyogo 650-0013, Japan

*E-mail: yamamoto.s.an@geo.titech.ac.jp

Received ; Accepted

Abstract

In most of mesh-free methods, the calculation of interactions between sample points or “particles” is the most time consuming. When we use mesh-free methods with high spatial orders, the order of the time integration should also be high. If we use usual Runge-Kutta schemes, we need to perform the interaction calculation multiple times per one time step. One way to reduce the number of interaction calculations is to use Hermite schemes, which use the time derivatives of the right hand side of differential equations, since Hermite schemes require smaller number of interaction calculations than RK schemes do to achieve the same order. In this paper, we construct a Hermite scheme for a mesh-free method with high spatial orders. We performed several numerical tests with fourth-order Hermite schemes and Runge-Kutta schemes. We found that, for both of Hermite and Runge-Kutta schemes, the overall error is determined by the error of spatial derivatives, for timesteps smaller than the stability limit. The calculation cost at the timestep size of the stability limit is smaller for Hermite schemes. Therefore, we conclude that Hermite schemes are more efficient than Runge-Kutta schemes and thus useful for high-order mesh-free methods for Lagrangian Hydrodynamics.

Key words: methods: numerical — hydrodynamics — planets and satellites: formation — galaxies:

1 Introduction

Lagrangian mesh-free methods, in which particles move following the motion of fluid, have been widely used for astrophysical hydrodynamical simulations. In most of mesh-free methods, the calculation of interactions between particles is the most time consuming part. Typically, one particle interacts with ~ 100 neighbor particles, and thus the cost of interaction calculations dominates the total calculation cost. One way to reduce the number of interaction calculations is to use Hermite schemes, which use the time derivatives of the right hand side of differential equations, since Hermite schemes require smaller number of interaction calculations than RK schemes do to achieve the same order.

In the field of stellar dynamics, the fourth order Hermite scheme (Makino 1991; Makino & Aarseth 1992) is widely used for high-order integration. The basic idea of the Hermite scheme is to calculate the time derivative of gravitational acceleration directly, and use it to construct high-order interpolation polynomial. If we calculate up to p -th order time derivative directly, we can achieve the order of $s(p+1)$ when we use s -step linear multistep method, and in the case of $s=2$, we can achieve the order of $2(p+1)$. The two-step linear multistep method can be formulated so that it requires only one force evaluation per timestep. In the case of grid-based scheme for hydrodynamics, Aoki (1997) described the method based purely on the Taylor expansion, which achieves order $p+1$.

In this paper, we combine the Hermite scheme with Consistent Particle Hydrodynamics in Strong Form (CPHSF; Yamamoto & Makino 2017) which is one of high-order mesh-free methods. One disadvantage of the Hermite scheme is that, even though it requires smaller number of interaction calculation, the calculation cost of one interaction is higher because we need to calculate high-order derivations. In the case of CPHSF or other MLS-based interpolation, high-order interpolation polynomial gives spatial derivatives, and we only need to convert spatial derivatives to time derivations using the original differential equations. Thus, the increase of the calculation cost is small and independent of the number of neighbors.

We performed several numerical tests. Fourth-order Hermite schemes and second- and fourth-order Runge-Kutta schemes are used for the test with a periodic boundary, and an implicit Hermite scheme, an implicit fourth-order Runge-Kutta scheme and the backward-Euler scheme are used for

* Example: Present Address is xxxxxxxxxx

the test with boundary conditions. We found that, for both of Hermite and Runge-Kutta schemes, the overall error is determined by the error of spatial derivatives, for timesteps smaller than the stability limit. The calculation cost at the timestep size of the stability limit is smaller for Hermite schemes. Therefore, we conclude that Hermite schemes are more efficient than Runge-Kutta schemes and thus useful for high-order mesh-free methods for Lagrangian Hydrodynamics.

In the rest of this paper, we first present the formulation of the Hermite scheme for CPHSF in section 2, and report the results of numerical tests in section 3. We summarize our study in section 4.

2 Derivation of the high-order scheme

In this section, we present the derivation of the fourth-order Hermite schemes for CPHSF.

2.1 Hermite scheme

In this section we present the formulation of the fourth-order Hermite schemes (Makino 1991; Makino & Aarseth 1992). Consider a second-order differential equation,

$$\frac{d\mathbf{x}}{dt} = \mathbf{v}, \quad (1)$$

$$\frac{d\mathbf{v}}{dt} = \mathbf{a}(\mathbf{x}). \quad (2)$$

Here, \mathbf{x} and \mathbf{v} denote the position and velocity of one particle. The fourth-order Hermite scheme is derived as follows. The predictor at time t_n is given by

$$\mathbf{x}_p = \mathbf{x}_n + \mathbf{v}_n \Delta t + \frac{\mathbf{a}_n}{2} \Delta t^2 + \frac{\dot{\mathbf{j}}_n}{6} \Delta t^3, \quad (3)$$

$$\mathbf{v}_p = \mathbf{v}_n + \mathbf{a}_n \Delta t + \frac{\dot{\mathbf{j}}_n}{2} \Delta t^2, \quad (4)$$

where \mathbf{x}_p and \mathbf{v}_p are the predicted position and velocity at the new time, $t_{n+1} = t_n + \Delta t$, \mathbf{x}_n and \mathbf{v}_n are the position and velocity at time t_n , and \mathbf{a}_n and $\dot{\mathbf{j}}_n$ are the acceleration and jerk (first time derivative of acceleration) at time t_n . Using \mathbf{x}_p and \mathbf{v}_p , we can now calculate the acceleration and jerk, \mathbf{a}_{n+1} and $\dot{\mathbf{j}}_{n+1}$, at time t_{n+1} . Using \mathbf{a}_n , $\dot{\mathbf{j}}_n$, \mathbf{a}_{n+1} and $\dot{\mathbf{j}}_{n+1}$, we can construct the third-order Hermite interpolation polynomial for $\mathbf{a}(t)$ as

$$\mathbf{a}(t) = \mathbf{a}_n + \dot{\mathbf{j}}_n(t - t_n) + \frac{\mathbf{s}_n}{2}(t - t_n)^2 + \frac{\mathbf{c}_n}{6}(t - t_n)^3, \quad (5)$$

where \mathbf{s}_n and \mathbf{c}_n are given by

$$\mathbf{s}_n = \frac{-6(\mathbf{a}_n - \mathbf{a}_{n+1}) - \Delta t(4\dot{\mathbf{j}}_n + 2\dot{\mathbf{j}}_{n+1})}{\Delta t^2}, \quad (6)$$

$$\mathbf{c}_n = \frac{12(\mathbf{a}_n - \mathbf{a}_{n+1}) + 6\Delta t(\dot{\mathbf{j}}_n + \dot{\mathbf{j}}_{n+1})}{\Delta t^3}. \quad (7)$$

We integrate equation (5) from t_n to t_{n+1} and obtain correctors given by

$$\mathbf{x}_c = \mathbf{x}_p + \frac{\mathbf{s}_n}{24}\Delta t^4 + \frac{\mathbf{c}_n}{120}\Delta t^5, \quad (8)$$

$$\mathbf{v}_c = \mathbf{v}_p + \frac{\mathbf{s}_n}{6}\Delta t^3 + \frac{\mathbf{c}_n}{24}\Delta t^4. \quad (9)$$

If we set $\mathbf{x}_{n+1} = \mathbf{x}_c$ and $\mathbf{v}_{n+1} = \mathbf{v}_c$ at this point, that means we use the PEC (predict-evaluate-correct) form of the linear multistep method. We can also use PECE or P(EC)² forms.

2.2 Derivation of high-order time derivatives for hydrodynamical equations

In this section, we describe how we calculate high-order time derivatives for hydrodynamics equations in Lagrangian view. Our approach is essentially the same as that of Aoki (1997), who derived higher-order time derivatives for Eulerian view. Aoki (1997) considered the following equation:

$$\frac{\partial}{\partial t}f = \xi_x f, \quad (10)$$

where ξ_x is some linear operator. By taking time derivatives of both sides of equation (10), they derived a series of equations,

$$\frac{\partial^2}{\partial t^2}f = \xi_x \xi_x f, \quad (11)$$

$$\frac{\partial^3}{\partial t^3}f = \xi_x \xi_x \xi_x f, \quad (12)$$

and so on. In this paper, we consider the equation

$$\frac{d}{dt}f = \xi_x f, \quad (13)$$

where d/dt is the Lagrangian derivative,

$$\frac{d}{dt} = \frac{\partial}{\partial t} + \mathbf{v} \cdot \nabla. \quad (14)$$

The original set of partial differential equations of a Lagrangian formulation of hydrodynamics is given by

$$\frac{d\rho}{dt} = -\rho \nabla \cdot \mathbf{v}, \quad (15)$$

$$\frac{d\mathbf{v}}{dt} = -\frac{\nabla P}{\rho}, \quad (16)$$

$$\frac{du}{dt} = -\frac{P}{\rho} \nabla \cdot \mathbf{v}, \quad (17)$$

$$P = P(\rho, u). \quad (18)$$

Here, we rewrite $(d/dt)(\nabla)$ as

$$\frac{d}{dt}\nabla = \nabla \frac{d}{dt} - \diamond. \quad (19)$$

The operator \diamond is defined as

$$\diamond_\alpha = (\nabla_\alpha v_\beta)(\nabla_\beta), \quad (20)$$

where α and β are indices of dimensions, and

$$\nabla_\alpha = \frac{\partial}{\partial x_\alpha}, \quad (21)$$

where $\alpha = 1, 2$ and 3 , and $\mathbf{x} = (x_1, x_2, x_3) = (x, y, z)$. The index β is summed over. Second time derivatives of ρ , \mathbf{v} and u are then expressed as

$$\frac{d^2\rho}{dt^2} = \rho(\nabla \cdot \mathbf{v})^2 + \rho \diamond \cdot \mathbf{v} + \Delta P - \frac{\nabla \rho \cdot \nabla P}{\rho}, \quad (22)$$

$$\frac{d^2\mathbf{v}}{dt^2} = \frac{1}{\rho} \nabla [\tilde{P}(\nabla \cdot \mathbf{v})] + \frac{\diamond P}{\rho} - \frac{(\nabla \cdot \mathbf{v})(\nabla P)}{\rho}, \quad (23)$$

$$\frac{d^2u}{dt^2} = \left(\frac{\tilde{P} - P}{\rho} \right) (\nabla \cdot \mathbf{v})^2 + \frac{P\Delta P}{\rho^2} - \frac{P(\nabla P) \cdot (\nabla \rho)}{\rho^3} + \frac{P \diamond \cdot \mathbf{v}}{\rho}, \quad (24)$$

where \tilde{P} is defined as

$$\tilde{P} \equiv \frac{P}{\rho} \frac{\partial P}{\partial u} + \rho \frac{\partial P}{\partial \rho}. \quad (25)$$

For the equation of state for ideal gas used in section 3.1,

$$P = (\gamma - 1)\rho u, \quad (26)$$

where γ is the ratio of specific heat, \tilde{P} is given by

$$\tilde{P} = \gamma P. \quad (27)$$

For the equation of state for weakly compressible fluid used in section 3.2,

$$P = c_0^2(\rho - \rho_{\text{air}}) + P_{\text{air}}, \quad (28)$$

where ρ_{air} , P_{air} , g , H and c_0 are air density, air pressure, gravity, height of fluid and sound velocity.

We set

$$c_0 = \sqrt{gH}. \quad (29)$$

The parameter \tilde{P} is given by

$$\tilde{P} = c_0^2 \rho. \quad (30)$$

In this paper, we apply artificial viscosity of the form the same as that in Yamamoto & Makino (2017). Note that we do not calculate the contribution of the artificial viscosity to the second time derivatives since artificial viscosity is not differentiable. Therefore, the artificial viscosity for PEC and P(EC) $^\infty$ forms of Hermite schemes are integrated with the Heun's scheme and the trapezoidal scheme, respectively. We calculate artificial viscosity as follows.

$$\frac{d\mathbf{v}}{dt} = -\frac{\nabla q}{\rho}, \quad (31)$$

$$\frac{du}{dt} = -\frac{q}{\rho} \nabla \cdot \mathbf{v}, \quad (32)$$

$$q = -\left(\frac{|\sum_m \lambda_m|}{\sum_m |\lambda_m|}\right)^2 \zeta \left[\alpha_{AV} \rho c_s h_{AV} + \beta_{AV} \rho h_{AV}^2 |\lambda_{mmax}| \right] \lambda_{mmax} \Theta(-\nabla \cdot \mathbf{v}), \quad (33)$$

where α_{AV} , β_{AV} and h_{AV} are coefficients, and c_s and ζ are the sound velocity and a parameter which controls the overall strength of AV. In this paper, we set $\alpha_{AV} = 1$ and $\beta_{AV} = 2$. The parameters λ_m are the eigenvalues of the strain rate tensor \mathbf{s} defined as

$$s_{\alpha,\beta} = \frac{1}{2} \left(\frac{\partial v_\alpha}{\partial x_\beta} + \frac{\partial v_\beta}{\partial x_\alpha} \right). \quad (34)$$

The parameter λ_{mmax} is the negative eigenvalue with the maximum absolute value. If all eigenvalues are non-negative, $q = 0$. In this paper, we use the time-independent coefficient ζ . We set $\zeta = 1$.

2.3 Calculation cost for time high order derivatives

For the fourth-order Hermite time integrations, we must derive second spatial order derivatives of physical quantities to calculate jerk, snap and crackle. However, if we use spatial high-order mesh-free methods (e.g., CPHSF), the additional number of arithmetic operations of jerk, snap and crackle is much smaller than the original number of the calculations of the spatial high-order mesh-free method.

In this section, we compare the original number of arithmetic operations and the additional number of the operations necessary for the Hermite scheme. First, we show how to derive the spatial high-order derivatives of a physical quantity f . Second, the original number of arithmetic operations of CPHSF is derived. We call this value N_{op} . Note that we assume that N_{op} comprises only the number of operations for the evaluation of the inverse matrix of B_i in equation (35) and interaction calculation between particles since these dominate the total calculation cost of CPHSF. Thirdly, the additional number of arithmetic operations for jerk, snap and crackle is derived. We call this value N_{add} . Finally, we compare N_{op} and N_{add} . To obtain the number of arithmetic operations, we calculate the number of floating-point operations per one particle of CPHSF. If a quantity have been derived, we assume that it will not be unnecessarily recalculated. We assume that the numbers of floating-point operations required to evaluate division and square root are both 20.

First, we show how to derive the spatial high-order derivatives of f . In CPHSF, the m -th spatial order derivatives of f is given by the following equations,

$$\delta^m f = \sum_\alpha \left[B_i^{-1} \right]_{m\alpha} \sum_j f_j p_{\alpha,ij} W_{ij}, \quad (35)$$

$$\boldsymbol{\delta} = \left(1, \nabla_x, \nabla_y, \nabla_z, \frac{1}{2}\nabla_x^2, \nabla_x\nabla_y, \dots, \nabla_y\nabla_z^{n_p-1}, \nabla_z^{n_p} \right)^T, \quad (36)$$

$$\mathbf{p}_{ij} = \left(1, x_{ij}, y_{ij}, z_{ij}, x_{ij}^2, x_{ij}y_{ij}, \dots, y_{ij}z_{ij}^{n_p-1}, z_{ij}^{n_p} \right)^T, \quad (37)$$

$$B_i = \sum_j W_{ij} \mathbf{p}_{ij} \otimes \mathbf{p}_{ij}, \quad (38)$$

where i and j are indices of particles, m and α are integers, n_p and W_{ij} are the spatial order of the scheme and a Kernel function and x_{ij} , y_{ij} and z_{ij} are $x_j - x_i$, $y_j - y_i$ and $z_j - z_i$.

In CPHSF, the total number of floating point operations per one neighbor particle is given by

$$N_{\text{op}} = N_{\text{int}}N_{\text{nb}} + N_{\text{inv}}, \quad (39)$$

where N_{nb} is the number of neighbor particles, and N_{int} and N_{inv} are the numbers of floating-point operations for interaction calculation between particles and the evaluation of the inverse matrix of B_i in equation (35). The number of floating-point operations for interaction calculation is given by

$$N_{\text{int}} = N_{\text{dist}} + N_{\text{kernel}} + N_{\text{sf}}, \quad (40)$$

where N_{dist} and N_{kernel} are the number of floating-point operations necessary to evaluate the relative distance and the kernel function. The last term, N_{sf} , represent the number of floating-point operations for the CPHSF fitting. In CPHSF, first of all, we evaluate only $|\mathbf{x}_{ij}|/h_i$, where \mathbf{x}_{ij} is the displacement of particle i and particle j and h_i is the Kernel length of particle i , to search neighbor particles of particle i , and N_{dist} are $\simeq 22$, 45 and 48 for 1, 2 and 3 dimensions. Then, we evaluate elements of B_i given by equation (38), polynomial equation given by equation (37) and kernel function W_{ij} to calculate equation (35). One interaction calculation between particle i and particle j in $[B_i]_{\alpha\beta}$ is given by $\{[p_{ij}]_{\alpha}[p_{ij}]_{\beta}W_{ij}\}$. The number of combinations of $[p_{ij}]_{\alpha}[p_{ij}]_{\beta}$ is $n(2n_p, D)$. The parameter $n(2n_p, D)$ is the number of bases of a polynomial fitting in equation (35), where D is the number of dimensions, and the value of $n(2n_p, D)$ is given by

$$n(2n_p, D) = \frac{1}{D!} \prod_{m=0}^{D-1} (n_p + m). \quad (41)$$

For example, if we consider one dimensional case, $\{[p_{ij}]_{\alpha}[p_{ij}]_{\beta}W_{ij}\}$ is given by $x_{ij}^{\alpha}x_{ij}^{\beta}W_{ij}$ and thus $[B_i]_{\alpha_1\beta_1}$ is the same as $[B_i]_{\alpha_2\beta_2}$ with $(\alpha_1 + \beta_1) = (\alpha_2 + \beta_2)$. Therefore, the number of the terms of the form of $\{[p_{ij}]_{\alpha}[p_{ij}]_{\beta}W_{ij}\}$ is $n(2n_p, D)$. Since we assume that a quantity, which have been derived, will not be unnecessarily recalculated, the number of floating-point operations for the evaluation of $\{[p_{ij}]_{\alpha}[p_{ij}]_{\beta}W_{ij}\}$ except for $\{[p_{ij}]_0[p_{ij}]_0W_{ij}\}$ is 1. For example, if we consider one dimensional case, we can get $x_{ij}^m W_{ij}$ by multiplying $x_{ij}^{m-1} W_{ij}$ by x_{ij} and thus the number of floating-point operations is only 1 for the evaluation of $x_{ij}^m W_{ij}$. In addition, the number of floating-point operations for summing each term $\{[p_{ij}]_{\alpha}[p_{ij}]_{\beta}W_{ij}\}$ with respect to j is 1. Therefore, the total number of floating-point op-

erations for one interaction calculation in B_i is $2n(2n_p, D) - 1$. One interaction calculation between particle i and particle j in the calculation of equation (35) is given by $W_{ij}f_j\mathbf{p}_{ij}$. The number of the terms of the form of $W_{ij}f_j[p_{ij}]_\alpha$ is $n(n_p, D)$. We have density (pressure), energy and velocity, and thus the number of physical quantities is $(D + 2)$. Therefore, the total number of floating-point operations for one interaction calculation in m -th derivatives of density (pressure), energy and velocity given equation (35) is $2(D + 2)n(n_p, D)$. Therefore, the number of floating-point operations for the CPHSF fitting is given by

$$N_{\text{sf}}(n_p, D) = 2n(2n_p, D) + 2(D + 2)n(n_p, D) - 1 \quad (42)$$

The numbers of floating-point operations that is necessary to evaluate the kernel function, N_{kernel} are $\simeq 33$, 35 and 36 for 1, 2 and 3 dimensions. From the above, the total numbers of floating-point operations for the calculation of equation (35) are $\simeq [33 + N_{\text{sf}}(n_p, 1)]$, $\simeq [35 + N_{\text{sf}}(n_p, 2)]$ and $\simeq [36 + N_{\text{sf}}(n_p, 3)]$ for 1, 2 and 3 dimensions.

From the above, the total numbers of floating-point operations for one interaction calculation of CPHSF, N_{int} , are

$$N_{\text{int}} \simeq [55 + N_{\text{sf}}(n_p, 1)], \quad (43)$$

$$N_{\text{int}} \simeq [80 + N_{\text{sf}}(n_p, 2)], \quad (44)$$

$$N_{\text{int}} \simeq [84 + N_{\text{sf}}(n_p, 3)], \quad (45)$$

for 1, 2 and 3 dimensions. Table 1 shows the summary of the numbers of floating-point operations for one interaction calculation of CPHSF.

Table 1. The numbers of floating-point operations for one interaction calculation of CPHSF

Process	$D = 1$	$D = 2$	$D = 3$
N_{dist}	$\simeq 22$	$\simeq 45$	$\simeq 48$
N_{kernel}	$\simeq 33$	$\simeq 35$	$\simeq 36$
N_{sf}	$N_{\text{sf}}(n_p, 1)$	$N_{\text{sf}}(n_p, 2)$	$N_{\text{sf}}(n_p, 3)$
Total	$\simeq [55 + N_{\text{sf}}(n_p, 1)]$	$\simeq [80 + N_{\text{sf}}(n_p, 2)]$	$\simeq [84 + N_{\text{sf}}(n_p, 3)]$

The evaluation of the inverse matrix of B_i also dominates in CPHSF and the number of floating-point operations of it, N_{inv} , is $\simeq 2n(n_p, D)^3/3$. Therefore, the numbers of floating-point operations per one particle of CPHSF are

$$N_{\text{op}} \simeq N_{\text{nb}}[55 + N_{\text{sf}}(n_p, 1)] + \frac{2}{3}n(n_p, 1)^3, \quad (46)$$

$$N_{\text{op}} \simeq N_{\text{nb}}[80 + N_{\text{sf}}(n_p, 2)] + \frac{2}{3}n(n_p, 2)^3, \quad (47)$$

$$N_{\text{op}} \simeq N_{\text{nb}}[84 + N_{\text{sf}}(n_p, 3)] + \frac{2}{3}n(n_p, 3)^3, \quad (48)$$

for 1, 2 and 3 dimension.

In the following, we derive N_{add} . To derive jerk, snap and crackle in the Hermite schemes, we need to calculate second spatial order derivatives of f_i given by equation (35). Here, the values of $\sum_j f_j p_{\alpha, ij} W_{ij}$ and $[B_i^{-1}]_{m\alpha}$ have been calculated in the derivation of the spatial first order derivative. Therefore, we must calculate only the multiplication of $[B_i^{-1}]_{m\alpha}$ by $\sum_j f_j p_{\alpha, ij} W_{ij}$ and the additional number of calculations for one physical quantity is given by ${}_D H_2 n(n_p, D)$. We have density (pressure), energy and velocity, and thus the number of physical quantities in a numerical calculation is $(D + 2)$. Therefore, the total additional number of calculations is $N_{\text{add}} = (D + 2) {}_D H_2 n(n_p, D)$.

Figure 1 shows N_{op} and N_{add} with respect to n_p . We assume $N_{\text{nb}} = 10, 75$ and 600 for 1, 2 and 3 dimensions. We can see that N_{add} is much smaller than N_{op} . Therefore, we conclude that the additional number of the calculations of jerk, snap and crackle is much smaller than the original number of the calculations of CPHSF.

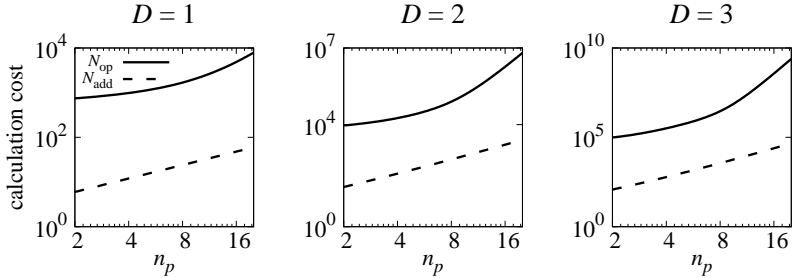


Fig. 1. The panels show the values of N_{add} and N_{op} plotted against n_p . The dashed and solid lines show these values for N_{add} and N_{op} . From left to right, the values of D are 1, 2 and 3.

3 Numerical Experiments

In this section, we present the result of the Sod shock tube test in section 3.1 and that for the test of the surface gravity wave in section 3.2. We compare the results of fourth-order Hermite schemes and second and fourth-order Runge-Kutta schemes in the Sod shock tube test, and the results of an fully implicit Hermite-scheme, the implicit fourth-order Runge-Kutta scheme and the backward-Euler scheme in the surface gravity wave test.

3.1 Sod shock tube

In this section, we present the result of the Sod shock tube test (Sod 1978). We assume that fluid is ideal gas with $\gamma = 1.4$. The computational domain is $-0.5 \leq x < 0.5$ with a periodic boundary, and initial boundary of two fluids are at $x = -0.5$ and 0 . In this test, we used equal-mass particles. Initial velocity is given by $v_x = 0$. The density is smoothed by a C^5 polynomial, and is given by

$$\rho(x) = \begin{cases} \rho_h & -0.25 \leq x < -x_0, \\ \frac{\rho_h - \rho_l}{2} \sum_{m=0}^5 b_m x^{2m+1} + \frac{\rho_h + \rho_l}{2} & -x_0 \leq x < x_0, \\ \rho_l & x_0 \leq x \leq 0.25, \end{cases} \quad (49)$$

where $(b_0, b_1, b_2, b_3, b_4, b_5) = (-693/256, 1155/256, -693/128, 495/128, -385/256, 63/256)$ and ρ_h and ρ_l are the values of initial density in the high- and low-density regions. We used $\rho_h = 1$ and $\rho_l = 0.25$. The parameter x_0 represents the width of the smoothing region, and we used two values of x_0 . One is an initial condition with $x_0 = 0.006$, and the other is a smooth initial condition with $x_0 = 0.03$. We set the initial condition for $0.25 \leq x < 0.5$ to be mirroring that of $0 < x \leq 0.25$, and $-0.5 \leq x \leq -0.25$ as mirroring $-0.25 \leq x \leq 0$. The positions of particles in the smoothing region are determined so that position x_i of particle i satisfies

$$\int_{x_{i-1}}^{x_i} \rho(x) dx = \frac{1}{2N_h}, \quad (50)$$

where N_h is the number of particles in the high-density region and the right-hand side of equation (50) is mass of a particle. The smoothed pressure is given by

$$P(x) = \begin{cases} P_h & -0.25 \leq x < -x_0, \\ \frac{P_h - P_l}{2} \sum_{m=0}^5 b_m x^{2m+1} + \frac{P_h + P_l}{2} & -x_0 \leq x < x_0, \\ P_l & x_0 \leq x \leq 0.25, \end{cases} \quad (51)$$

where P_h and P_l are the values of initial pressure in the high- and low-density regions. We used $P_h = 1$ and $P_l = 0.1795$. We used equations (31) and (32) for the artificial viscosity with $h_{AV} = 2.375 \times 10^{-3}$. We used a sixth-order interpolation with the value of interpolation polynomial at the position of particle x_i fixed to the actual value. Therefore, δ given by equation (36) and p_{ij} given by equation (37) are

$$\delta = \left(1, \nabla_x, \frac{1}{2!} \nabla_x^2, \frac{1}{3!} \nabla_x^3, \frac{1}{4!} \nabla_x^4, \frac{1}{5!} \nabla_x^5 \right)^T, \quad (52)$$

$$p_{ij} = \left(1, x_{ij}, x_{ij}^2, x_{ij}^3, x_{ij}^4, x_{ij}^5 \right)^T. \quad (53)$$

The kernel function is the fourth-order Wendland function (Wendland 1995). The kernel length is given by

$$h_i = \eta \left(\frac{\tilde{m}_i}{\rho_i} \right)^{1/D}, \quad (54)$$

$$\tilde{m}_i = \rho_{t=0,i} \Delta V_{t=0,i}, \quad (55)$$

where $\rho_{t=0,i}$ and $\Delta V_{t=0,i}$ are density and geometric volume of a particle i at $t = 0$. We set $\eta = 3.8$.

We calculated L1-norm error of density at $t = 0.1$ to verify the spatial order of the schemes and to compare the accuracy of the schemes,

$$\epsilon_\rho = \sum_{n=1}^{N_x} \frac{1}{N_x} \frac{|\rho_n - \rho_n^{\text{hres}}|}{\rho_n^{\text{hres}}}, \quad (56)$$

where ρ_n^{hres} is the result of a high-resolution test in which the number of particles, N_x , is 8000 and $dt = 10^{-6}$. When we derived equation (56), we calculated ρ_n of particles rearranged at positions same as those of the high-resolution test. The time integrator for high-resolution test is the Hermite scheme of the P(EC)² form. For the test of the time order of the scheme for the test with $N_x = N_0$, $\rho_{n,\Delta t}^{\text{hres}}$ is the result of a high-resolution test in which N_x is N_0 and $dt = 10^{-6}$. The time integrator for high-resolution test is the same as that for ρ_n . In this case we define the error as

$$\epsilon_{\rho,\Delta t} = \sum_{n=1}^{N_x} \frac{1}{N_x} \frac{|\rho_n - \rho_{n,\Delta t}^{\text{hres}}|}{\rho_{n,\Delta t}^{\text{hres}}}, \quad (57)$$

We compare results with PEC, PECE and P(EC)² forms of Hermite schemes, and Heun's scheme (hereafter RK2) and the classical fourth-order Runge-Kutta scheme (hereafter RK4). The numbers of particles, N_x , are 1000, 2000 and 4000.

Figure 2 shows density profiles at $t = 0.1$ for the tests with $N_x = 1000$ and $dt \simeq dt_{\text{max}}/4$, where dt_{max} is the maximum time step in the stability region, with the PEC form of the Hermite scheme. Note that the results for all schemes are similar to that for the PEC form of the Hermite scheme. We can see that the shock wave can be captured. However, the post shock oscillation is strong for $x_0 = 0.006$. Figures 3 is the same as figure 2, but for $N_x = 4000$. Note that the results are independent of the time integration scheme used and the results for $N_x = 2000$ are similar to those for $N_x = 4000$. We can see that the shock wave can be captured clearly even if initial condition is not smooth. Therefore, if the initial condition is not smooth, the resolution of time and space should be higher.

Now we check the spatial order of the scheme. We used the sixth order shape function and then the first and second derivatives are fifth and fourth orders in space. Therefore, if the result converges to an exact solution following the order of the method, the order of the scheme should be larger than or equal to four and thus ϵ_ρ should be given by $\epsilon_\rho \propto N_x^{-m}$ where m is larger than or equal to 4. Figure 4 shows that ϵ_ρ for the P(EC)² form of the Hermite scheme for runs with $dt = 10^{-6}$ plotted against N_x^{-1} . The results are independent of the time integration scheme used. The value of ϵ_ρ for runs with $x_0 = 0.006$ is proportional to N_x^{-4} . The value of ϵ_ρ in the large N_x region for runs with $x_0 = 0.03$ is proportional to N_x^{-1} since, in this region, the round-off error dominates the total error. In the other

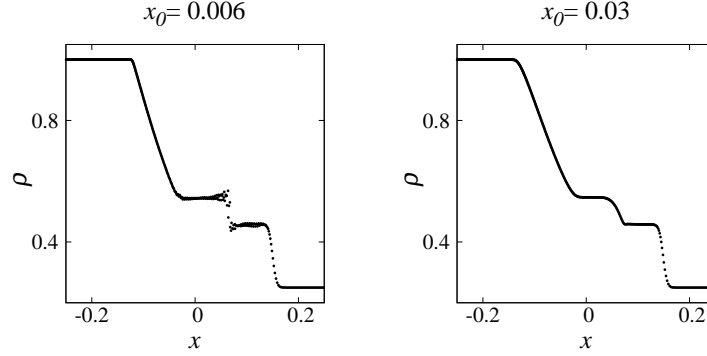


Fig. 2. The results of the Sod shock tube tests with $N_x = 1000$. The density profiles at $t = 0.1$ are shown. The left and right panels show the results for $x_0 = 0.006$ and $x_0 = 0.03$.

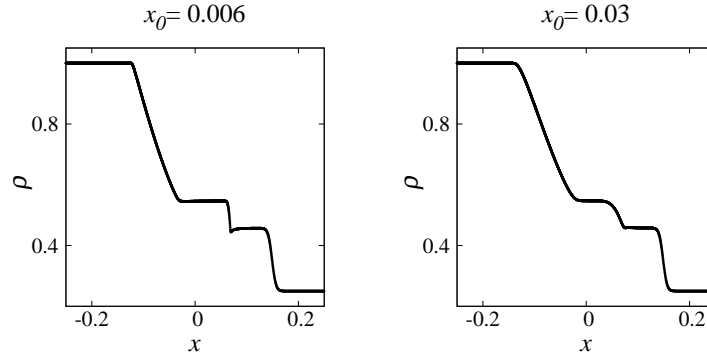


Fig. 3. The same as figure 2, but for $N_x = 4000$.

region, ϵ_ρ is proportional to N_x^{-4} . From these results, we can conclude that the spatial order of the scheme is consistent to theoretical expectation.

Let us look at the time orders of the schemes. Figures 5 and 6 show $\epsilon_{\rho, \Delta t}$ for the tests with $x_0 = 0.006$ and $x_0 = 0.03$ plotted against dt_{ic} where dt_{ic} is dt divided by the number of interaction calculations per one time step. We can see that the errors of RK2 and RK4 are $\mathcal{O}(dt^2)$ and $\mathcal{O}(dt^4)$ respectively, and that of the Hermite schemes are $\mathcal{O}(dt^2)$.

In the following we explain the reason why the order of the Hermite scheme is $\mathcal{O}(dt^2)$ for fixed

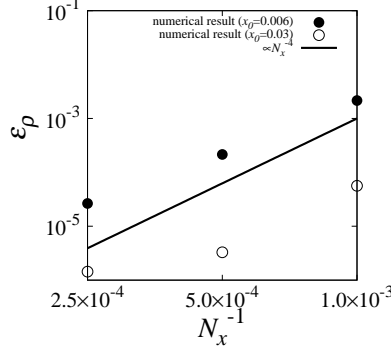


Fig. 4. The panel shows ϵ_ρ at $t = 0.1$ for the tests with $x_0 = 0.006$ and $x_0 = 0.03$ plotted against N_x^{-1} . Filled and open circles show results for $x_0 = 0.006$ and 0.03 , and solid curve shows the theoretical models for the error.

N_x^{-1} . In a particle-based method, the calculated spatial derivatives contain discretization errors, and therefore the time derivative contain errors. In the case of RK schemes, this error causes the solution in the limit of $dt \rightarrow 0$ to converge to the solution different from the exact solution, but the rate of the convergence is the order of the time integration scheme, since we can regard the space-discretized differential equations as the set of ordinal differential equations. However, in the case of the Hermite scheme, we construct the second time derivatives of physical quantities from the original equations and high-order spatial derivatives, and these spatial derivatives contain discretization errors. Thus, both the first and second time derivatives contain the errors due to space discretization errors, and therefore the second time derivatives are not exactly the time derivatives of the first time derivatives. For simplicity, let us illustrate this behaviour for the integration of velocity in one dimension. Here, we rewrite the correctors by substituting equations (6) and (7) to equation (9). Note that we set $dt = \Delta t$ in equation (4).

$$v_c = v_n + \frac{1}{2}(a_n + a_{n+1})\Delta t + \frac{1}{12}(j_n - j_{n+1})\Delta t^2. \quad (58)$$

If we use sixth order polynomial fitting for deriving spatial derivatives, v_c containing the spatial errors is given by

$$v_c = v_n + \frac{1}{2}(A_n + A_{n+1})\Delta t + \frac{1}{12}(J_n - J_{n+1})\Delta t^2, \quad (59)$$

where A_n , A_{n+1} , J_n and J_{n+1} are accelerations at n and $n + 1$ steps and jerks at n and $n + 1$ steps and are given by sixth order polynomial fitting for deriving spatial derivatives. Therefore, J is not equal to the time derivative of A .

$$J = \frac{dA}{dt} + \epsilon_J, \quad (60)$$

where ϵ_J is the error. Here, we integrate equation (59) from $t = 0$ to $t = T$,

$$\begin{aligned}
v_{c,(t=T)} &= v_{(t=0)} + \sum_{n=0}^{N_t} \left[\frac{1}{2} (A_n + A_{n+1}) \Delta t \right] + \sum_{n=0}^{N_t} \left[\frac{1}{12} (J_n - J_{n+1}) \Delta t^2 \right] \\
&= v_{(t=0)} + \sum_{n=0}^{N_t} \left[\frac{1}{2} (A_n + A_{n+1}) \Delta t \right] + \sum_{n=0}^{N_t} \left[\frac{1}{12} \left(\frac{dA_n}{dt} + \epsilon_{J,n} - \frac{dA_{n+1}}{dt} - \epsilon_{J,n+1} \right) \Delta t^2 \right],
\end{aligned} \tag{61}$$

where N_t is given by $N_t = T/\Delta t$. Here, we can assume that

$$\frac{dv}{dt} = \lim_{\Delta t \rightarrow 0} A. \tag{62}$$

Therefore, equation (61) becomes

$$v_{(t=T)} = v_A(T) + \mathcal{O}(\Delta t)^4 + \frac{1}{12} [\epsilon_{J,(t=0)} - \epsilon_{J,(t=T)}] \Delta t^2, \tag{63}$$

where $v_A(T)$ is the analytical solution for the velocity which satisfies equation (62). We can see that the time order of a Hermite scheme is equal to two. From these results, we can conclude that the time orders of the schemes are consistent. The fact that the apparent error order of the Hermite scheme is two does not imply it is a second order scheme, since when we simultaneously shrink the interparticle distance and timestep, the error will be $\mathcal{O}(dt^4)$ as expected. The second-order behaviour occurs only when the spatial error dominates the total error.

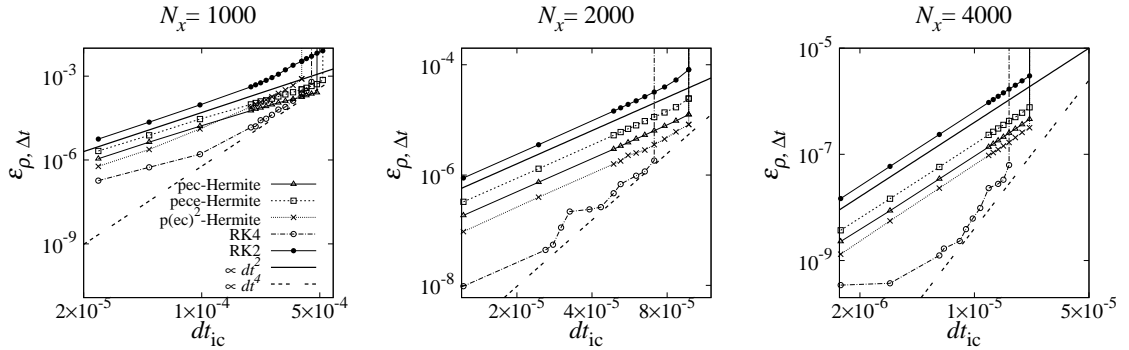


Fig. 5. The panel shows $\epsilon_{\rho, \Delta t}$ at $t = 0.1$ for the tests with $x_0 = 0.006$ plotted against dt_{ic} . From left to right panels, the results for the $N_x = 1000, 2000$ and 4000. The lower left and lower middle side panels show the results for the second and fourth Runge-Kutta schemes. Triangles, squares and crosses show the results for Hermite schemes in PEC, PECE, P(EC)² forms, and open and filled circles show the results for RK4 and RK2. Solid and dashed curves show the theoretical models for the error of second- and fourth-order schemes.

Figure 7 shows errors for tests with $x_0 = 0.006$ plotted against dt_{ic} . The result shows that the

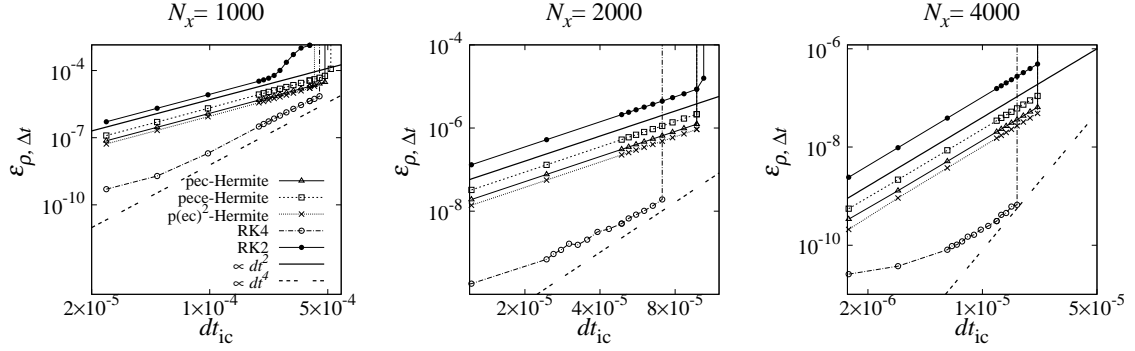


Fig. 6. Same as figure 5, but the results for $x_0 = 0.03$.

accuracy of fourth-order Hermite schemes is similar to those of RK2 and RK4, since the errors of spatial differentiation approximation determines the overall error.

Figure 8 shows maximum dt_{ic} in the numerical stable region for tests with $x_0 = 0.006$ plotted against N_x^{-1} . We can see that the regions of stability of fourth-order Hermite schemes are larger than or equal to those of RK2 and RK4. Hence, we can use larger timesteps with the Hermite schemes. Therefore, we can conclude that Hermite schemes, especially in PEC and PECE forms, are better than Runge-Kutta schemes for simulations of fluid with shock and contact discontinuity, even when the initial condition has sharp jump.

Figure 9 shows errors for $x_0 = 0.03$ plotted against dt_{ic} . As in the case of $x_0 = 0.006$, the results show that the accuracy of fourth-order Hermite schemes is similar to those of RK2 and RK4, since the errors of spatial differentiation approximation determines the overall error.

Figure 10 shows maximum dt_{ic} in the numerical stable region for tests with $x_0 = 0.03$ plotted against N_x^{-1} . As in the case of $x_0 = 0.006$, the results the regions of stability of fourth-order Hermite schemes are larger than or equal to those of RK2 and RK4. Therefore, we can conclude that Hermite schemes, especially in PEC and PECE forms, are better than Runge-Kutta schemes for simulations of fluid with shock and contact discontinuity. We can conclude that Hermite schemes are more computationally efficient better than Runge-Kutta schemes for calculation shocks.

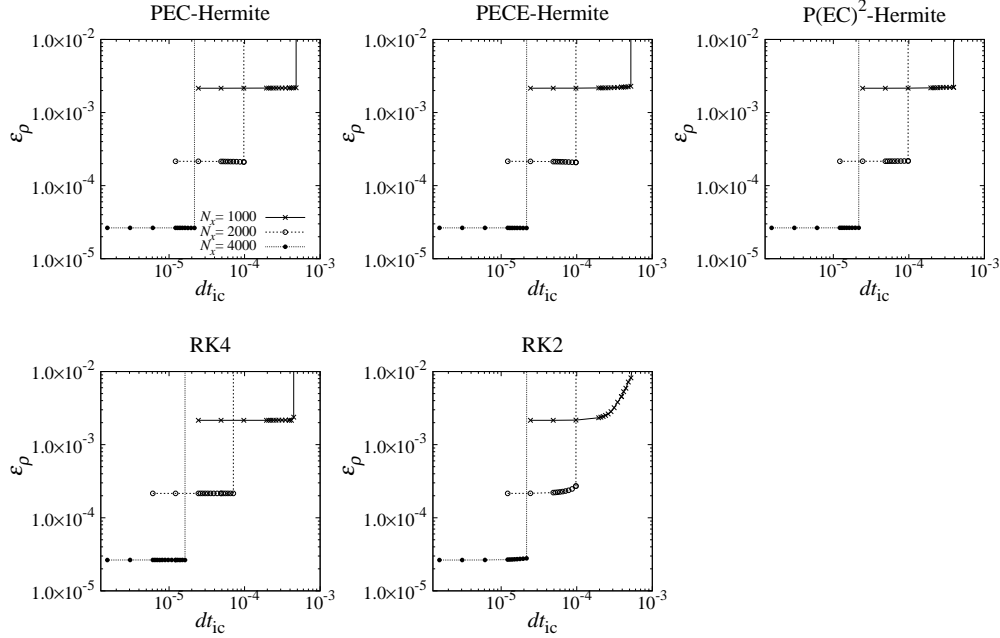


Fig. 7. The panel shows ϵ_ρ at $t = 0.1$ for the tests with $x_0 = 0.006$ plotted against dt_{ic} . From left to right in the upper panels, the results for the PEC-, PECE- and $P(EC)^2$ -Hermite schemes are shown. The lower left and lower middle side panels show the results for the second and fourth Runge-Kutta schemes. Crosses, open and filled circles show results for $N_x = 1000, 2000$ and 4000 .

3.2 Surface gravity wave test

The surface gravity wave test is useful for the investigation of the capability of numerical schemes to handle two-dimensional fluid dynamics with high accuracy and small dissipation. The initial condition is the same as those in Antuono et al. (2011) and Yamamoto & Makino (2017), but sound velocity given by equation (29) is 10 times smaller than that of Yamamoto & Makino (2017). We assume that fluid is weakly compressible with the equation of state given by equation (28) with $\rho_{\text{air}} = 10^3$ and $P_{\text{air}} = 10^5$ and sound velocity given by equation (29) with $g = -10$ and the height of fluid $H = 1$. The computational domain is $0 \leq x < 1, 0 \leq y \leq 1$. We applied a periodic boundary at $x = 0, v_y = 0$ at $y = 0$ and $P = P_{\text{air}}$ for particles initially at $y = 1$ as boundary conditions. Initial density is

$$\rho(y) = \rho_{\text{air}} e^{g(H-y)/c_0^2}. \quad (64)$$

Initial velocity is

$$v_x = A \frac{|g|k}{\omega} \frac{\cosh(ky)}{\cosh(kH)} \sin(kx), \quad (65)$$

$$v_y = -A \frac{|g|k}{\omega} \frac{\sinh(ky)}{\cosh(kH)} \cos(kx), \quad (66)$$

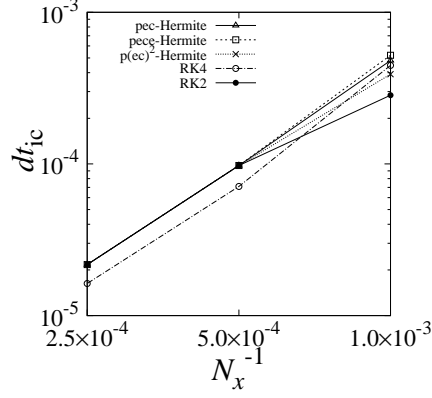


Fig. 8. The panels show maximum dt_{ic} in the numerical stable region for tests with $x_0 = 0.006$ plotted against N_x^{-1} . Triangles, squares and crosses show the results for Hermite schemes in PEC, PECE, P(EC)² forms, and open and filled circles show the results for RK4 and RK2.

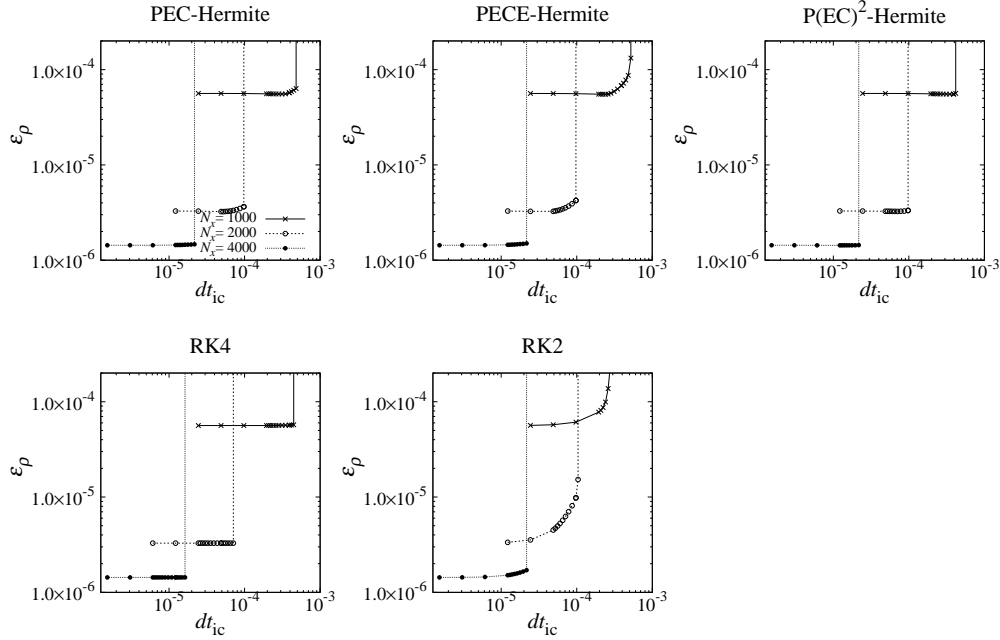


Fig. 9. The same as figure 7, but for $x_0 = 0.03$.

where A , k and ω are the amplitude, the number of wave and its frequency. We set $A = 0.01$, $k = 2\pi$ and $\omega = \sqrt{|g|k \tanh(kH)}$. In this test, we do not use artificial viscosity to clarify the origin of the error. We used a fifth-order interpolation with the value of interpolate polynomial at the position of particle x_i fixed to the actual value. Therefore, δ given by equation (36) and p_{ij} given by equation (37) are

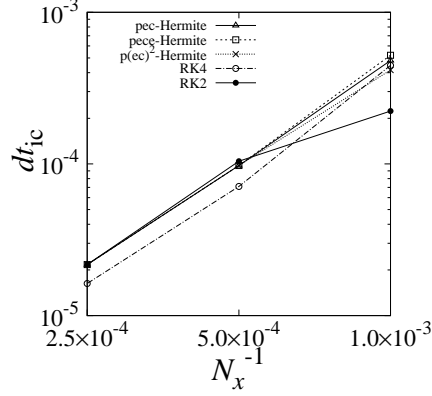


Fig. 10. The same as figure 8, but for $x_0 = 0.03$.

$$\boldsymbol{\delta} = \left(1, \nabla_x, \frac{1}{2!} \nabla_x^2, \nabla_x \nabla_y, \frac{1}{2!} \nabla_y^2, \dots, \frac{1}{2!3!} \nabla_x^2 \nabla_y^3, \frac{1}{4!} \nabla_x \nabla_y^4, \frac{1}{5!} \nabla_y^5 \right)^T, \quad (67)$$

$$\mathbf{p}_{ij} = \left(1, x_{ij}, y_{ij}, x_{ij}^2, x_{ij} y_{ij}, y_{ij}^2, \dots, x_{ij}^2 y_{ij}^3, x_{ij} y_{ij}^4, y_{ij}^5 \right)^T. \quad (68)$$

The kernel function is the fourth-order Wendland function (Wendland 1995). We used equation (54) as the kernel length and set $\eta = 3.8$.

We calculate the absolute error of v_x at $(x, y) = (0.4, 1)$ and $t = 0.2T$ where T is the period given by $2\pi/\omega$ for checking the spatial order of the schemes and comparing the accuracy of the schemes.

$$\epsilon_{v_x} = |v_x - v_x^{\text{hres}}|, \quad (69)$$

where v_x^{hres} is the result of the high-resolution test in which the number of particles, N , is 128×129 and $dt = T/1024$. The time integrator for high-resolution test is the implicit Hermite scheme. For checking the time order of the scheme for the test with $N = N_0$, $v_{x,\Delta t}^{\text{hres}}$ is the result of a high-resolution test in which N is N_0 and $dt = T/512$. The time integrator for high-resolution test is same as v_x . We calculated v_x and $v_{x,\Delta t}^{\text{hres}}$ of the particles initially at $(x, y) = (0.3125, 1)$. In this case we define the error as

$$\epsilon_{v_x,\Delta t} = |v_x - v_{x,\Delta t}^{\text{hres}}|, \quad (70)$$

We compare results of runs with the implicit Hermite scheme, the backward-Euler scheme (hereafter IRK1) and the Gauss-Legendre scheme (hereafter IRK4). The numbers of particles, N , are 16×17 , 32×33 and 64×65 .

Figure 11 shows the time evolution up to $t = 0.75T$ with the implicit Hermite scheme, $N = 16 \times 17$ and $dt \simeq dt_{\text{max}}/4$. Figure 12 shows y of the particle initially at $(x, y) = (0, 1)$ with the implicit

Hermite scheme, $N = 16 \times 17$ and $dt \simeq dt_{\max}/4$. Note that the results are independent of the time integration scheme used and N .

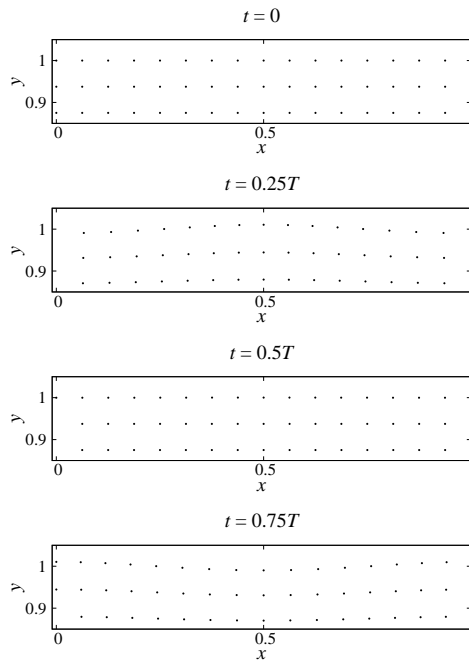


Fig. 11. Results of the surface gravity wave tests with $N = 16 \times 17$, from top to bottom, the snapshots at $t = 0, 0.25T, 0.5T$ and $0.75T$ are shown.

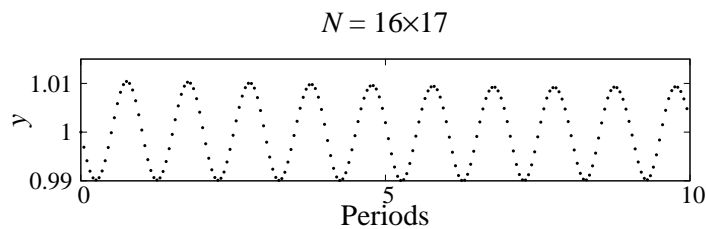


Fig. 12. Time evolution of the y -coordinate of the particle initially at $(x, y) = (0, 1)$ in the surface gravity wave test with $N = 16 \times 17$.

Now we check the spatial order of the scheme. We used the fifth order shape function and then the first and second derivatives are fourth and third orders in space. Therefore, if the result converges

to an exact solution following the order of the method, the order of the scheme should be larger than or equal to three and thus ϵ_{v_x} should be given by $\epsilon_{v_x} \propto N_x^{-m}$ where m is larger than or equal to 3 and N_x is the number of particles of the x -direction. Figure 13 shows ϵ_{v_x} for the implicit Hermite scheme with $dt = T/512$ plotted against N_x^{-1} . We can see that the error ϵ_{v_x} is proportional to N_x^{-4} . Therefore, the error in acceleration determines the overall error. The results are independent of the time integration used. From the result, the spatial order of the scheme is consistent.

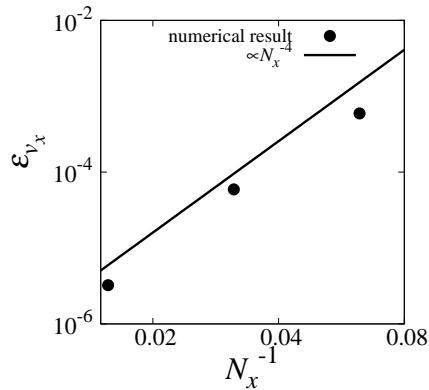


Fig. 13. The panel shows ϵ_{v_x} at $t = 0.2T$ plotted against N_x^{-1} . Filled circles show numerical results and solid curves show the theoretical models for the error.

Let us now look at the time order of the scheme. Figure 14 shows that $\epsilon_{v_x, \Delta t}$ plotted against dt_{ic} . We can see that the errors of the implicit Hermite scheme, IRK4 and IRK1 are $\mathcal{O}(dt^2)$, $\mathcal{O}(dt^4)$ and $\mathcal{O}(dt)$ respectively. As described in section 3.1, the time order of Hermite scheme is equal to two. From these results, we can conclude that the time orders of the schemes are consistent.

Figure 15 shows errors plotted against dt_{ic} . The result shows that the accuracy of the implicit Hermite scheme is similar to that of IRK4 and smaller than that of IRK1 with large N .

Figure 16 shows the maximum dt_{ic} in the numerical stable region plotted against N_x^{-1} . We can see that the region of stability of the implicit Hermite scheme are wider than those of IRK1 and IRK4. Hence, we can use larger timesteps with the implicit Hermite scheme. Therefore, we can conclude that the Hermite scheme is better than Runge-Kutta schemes for simulations of fluid with the surface and gravity wave.

4 Summary

If we use multi-stage integration schemes, such as Runge-Kutta schemes, with mesh-free methods we need to perform the interaction calculation, which is the most expensive part of the calculation,

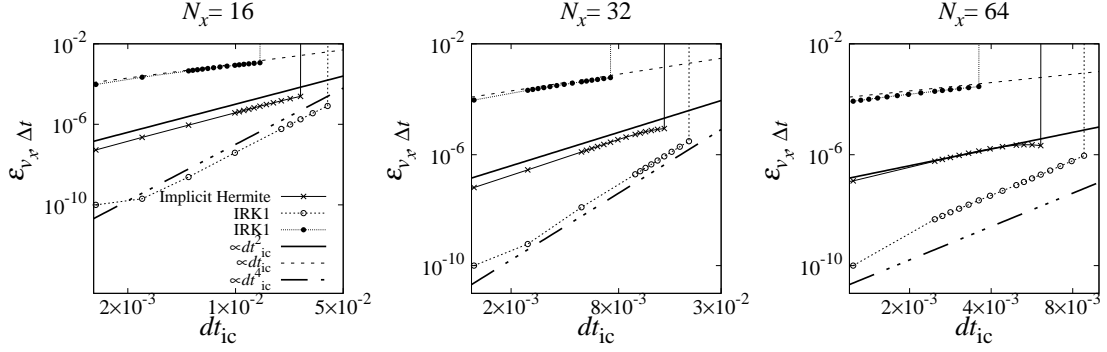


Fig. 14. The panel shows $\epsilon_{v_x, \Delta t}$ plotted against dt_{ic} . From left to right panels, the results for the $N_x = 16, 32$ and 64 . Crosses, open and filled circles show the results of the implicit Hermite scheme, IRK4 and IRK1. Dashed, solid and dot-dot-dashed curves show the theoretical models for the error of second-, first- and fourth-order schemes.

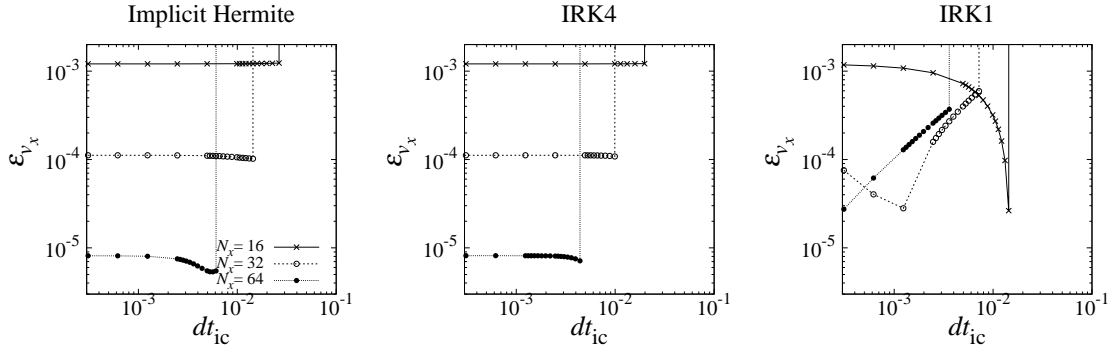


Fig. 15. The panel shows ϵ_{v_x} plotted against dt_{ic} . Left, middle and right sides panels show the results for implicit Hermite scheme, IRK4 and IRK1. Crosses, open and filled circles show results for $N_x = 16, 32$ and 64 .

multiple times per one time step. We constructed the Hermite scheme for a high-order mesh-free method. The accuracy of fourth-order Hermite schemes is at least similar to those of Runge-Kutta schemes and the region of stability of Hermite schemes are better than those of Runge-Kutta schemes. Therefore, we can use a large time step with the Hermite scheme compare to that for the Runge-Kutta scheme for the same accuracy. We conclude that Hermite schemes are more computationally efficient

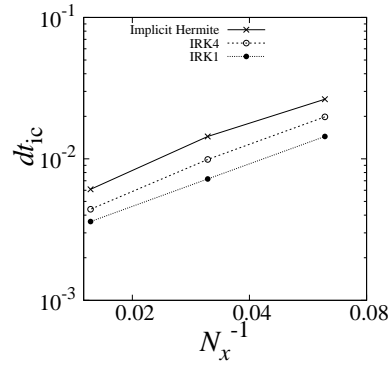


Fig. 16. The panels show maximum dt_{ic} in the numerical stable region for tests with $x_0 = 0.006$ plotted against N_x^{-1} . Crosses, open and filled circles show the results of the implicit Hermite scheme, IRK4 and IRK1.

than commonly used Runge-Kutta schemes for a high-order mesh-free method.

Acknowledgments

We would like to thank the referee for his or her insightful comments and suggestions. We also thank the editor for his or her assistance. We thank Masaki Iwasawa, Keigo Nitadori and Daisuke Namekata for discussions about Hermite schemes and Runge-Kutta schemes. This research was supported by RIKEN Junior Research Associate Program and MEXT as “Exploratory Challenge on Post-K computer” (Elucidation of the Birth of Exoplanets [Second Earth] and the Environmental Variations of Planets in the Solar System).

References

- Antuono, M., Colagrossi, A., Marrone, S., & Lugni, C. 2011, *Computer Physics Communications*, 182, 866
- Aoki, T. 1997, *Computer Physics Communications*, 102, 132
- Gingold, R. A., & Monaghan, J. J. 1977, *MNRAS*, 181, 375
- Makino, J. 1991, *ApJ*, 369, 200
- Makino, J., & Aarseth, S. J. 1992, *PASJ*, 44, 141
- Sod, G.A. 1978, *Journal of computational physics*, 27, 1
- Wendland, H. 1995, *Advances in computational Mathematics*, 4, 389.
- Yamamoto, S., & Makino, J. 2017, *PASJ*, 69.